

Surface-to-subsurface velocity projection for shallow water currents

Colin Y. Shen and Thomas E. Evans

Remote Sensing Division, Naval Research Laboratory, Washington, D. C.

Abstract. Sea surface currents in coastal oceans are accessible to continuous direct observations by shore-based high-frequency Doppler radar systems. Inferring current structure in shallow water from such surface current observations is attempted. The approach assumes frictionally dominated flow and vertically varying current velocity on the scale of the Ekman boundary layer. The approximation of the velocity variation with depth is consequently derivable in terms of orthogonal basis functions from the sea surface kinematic and dynamic boundary conditions; specifically, the viscous momentum and shear equations evaluated at the sea surface. The inference procedure developed is demonstrated with sea surface data obtained in the coastal High-Resolution Remote Sensing Experiment on the continental shelf off Cape Hatteras. Despite uncertainties in the surface measurements, qualitative agreement is obtained between the inferred subsurface current and the current measured in situ. The sensitivity of the inference to the measurement uncertainties as well as to the model assumptions is investigated, and the inferred result is found to be generally robust.

1. Introduction

The use of shore-based high-frequency (HF) Doppler radar to measure surface coastal currents has gained increasing acceptance in recent years (see, e.g., *Prandle*, 1991; *Shay et al.*, 1995; *Paduan and Rosenfeld*, 1996). The deployment of a pair of such radars at tens of kilometers apart can yield virtually continuous surface current velocity measurements at ~1 km resolution synoptically over an area of tens of kilometers square. This capability has rendered the HF radar useful for monitoring coastal currents, which often vary rapidly in response to local wind, tidal, and buoyancy forcing. The velocity field measured with the HF radar is, nevertheless, only a surface view of the total three-dimensional (3-D) current field. Downward from the surface, the speed and direction of the current can change significantly, as in the case of the Ekman spiral produced by a balance between the Coriolis and frictional forces.

However, in situations where the viscous dynamics dominates, as often happens in shallow coastal ocean water, the viscous diffusive transfer of momentum and shear downward from the surface, via eddy viscosity from turbulent mixing, necessarily dictates how the surface motion is coupled to the interior current. Thus it may be possible to infer the velocity change with depth in shallow water by considering the surface-to-subsurface eddy viscous coupling. With the measured surface current velocity and wind stress it is possible to estimate downward diffusion of momentum and shear near the sea surface from the equations of motion. In this study, the surface-to-subsurface viscous coupling indicated by downward momentum shear diffusion estimable at the sea surface will be exploited in an attempt to infer subsurface shallow water current structure from the surface data. It is clear that an inference based on the surface data can yield at best only an ap-

proximate view of the subsurface current. Nevertheless, the inference combined with the synoptic surface data provides a means to estimate the 3-D current structure that would otherwise be difficult to measure synoptically in situ. The viability of the inference approach presented here will be tested by applying it to actual data obtained from a coastal field experiment and comparing the inferred current structure with in situ velocity measurements.

The synoptic surface current velocity required to project the velocity downward can be obtained from the HF radar as already noted. The synoptic surface wind stress needed for estimating the surface vertical shear for use in the velocity projection can be obtained with existing remote sensing techniques such as airborne scatterometry. Alternatively, both the surface velocity and vertical shear may be measured with a single shore-based multifrequency radar system, as demonstrated recently [*Fernandez et al.*, 1996]. In theory, the sea surface height gradient is needed as well to specify the surface dynamics as discussed previously [*Shen*, 1997]. However, for homogeneous or weakly density-stratified shallow coastal water this requirement can be relaxed, as will be shown. The eddy viscosity required for the downward velocity projection will be determined as part of the solution procedure so that there is an internal consistency. Thus, with the present approach, prior knowledge of the sea surface height gradient and eddy viscosity value is not needed. Rather, these quantities and the velocity profile are obtained within a dynamically consistent framework.

In section 2, the equations of motion governing the surface current motion at the scale appropriate to the HF radar measurement are stated. In section 3, the eddy viscous diffusion terms in the governing equations for momentum and shear at the surface are obtained as constraints on the subsurface velocity profile. The uniform eddy viscosity model needed to achieve this is discussed. The dynamical constraints are supplemented by surface and bottom kinematic boundary conditions. In section 4, a vertical modal representation of the ve-

This paper is not subject to U.S. copyright. Published in 2001 by the American Geophysical Union.

Paper number 2000JC000267.

locity profile is introduced, and the solution procedure is described for obtaining the velocity profile, as well as the eddy viscosity values consistent with the profile, from the boundary constraints. In section 5, the surface velocities measured by the HF radar in a field experiment are used to infer the subsurface current, and the result is compared to the in situ current measurement. In section 6, conclusions are given.

2. Governing Equations

The horizontal scale of current motion resolved by the HF radar is typically >1 km. In shallow water of a few tens of meters depth, currents on this scale are essentially horizontal, and the vertical force balance on the currents can be approximated by the hydrostatic relation,

$$\frac{\partial P}{\partial z} = -g\rho, \quad (1)$$

where P is the pressure, g is the gravitational acceleration, ρ is the water density, and z is the vertical coordinate, positive upward.

The 2 orders of magnitude difference between the horizontal scale and the water depth also means that the vertical viscous process is most likely to dominate momentum diffusion since the magnitude of diffusive flux varies inversely with the length scale. Retaining only the vertical diffusion term, the horizontal momentum balance is thus

$$\frac{\partial \mathbf{u}}{\partial t} + \mathbf{u} \cdot \nabla \mathbf{u} + w \frac{\partial \mathbf{u}}{\partial z} + \mathbf{f} \times \mathbf{u} = -\frac{\nabla P}{\rho_0} + \frac{\partial}{\partial z} \left(\nu_e \frac{\partial \mathbf{u}}{\partial z} \right), \quad (2)$$

where $\mathbf{u} = (u, v)$ is the horizontal velocity vector, w is the vertical velocity, $\mathbf{f} = (0, 0, f)$ is the Coriolis frequency, $\nabla = (\partial/\partial x, \partial/\partial y)$ is the horizontal gradient operator, ν_e is the kinematic eddy viscosity, and ρ_0 is a constant reference density that comes from applying the Boussinesq approximation to (2).

Along the sea surface on which the pressure is constant the horizontal pressure gradient in (2) is proportional to the sea surface slope, i.e.,

$$\left[\frac{\nabla P}{\rho_0} \right]_{z=\eta} = g \frac{\bar{\rho}}{\rho_0} \nabla \eta, \quad (3)$$

by the hydrostatic relation (1), where η is the sea surface height and $\bar{\rho}$ is the water density at the sea surface. The total surface fluid acceleration in (2) can be cast in terms of the acceleration of the surface velocity $\bar{\mathbf{u}} = \mathbf{u}(x, y, z = \eta, t)$, or $\partial \bar{\mathbf{u}}/\partial t + \bar{\mathbf{u}} \cdot \nabla \bar{\mathbf{u}}$, since the free surface vertical velocity is $w(x, y, z = \eta, t) = \partial \eta/\partial t + \bar{\mathbf{u}} \cdot \nabla \eta$. In terms of $\bar{\mathbf{u}}$ and (3) the surface momentum equations governing the current motion measured by an ocean surface current radar (OSCR) is,

$$\frac{\partial \bar{\mathbf{u}}}{\partial t} + \bar{\mathbf{u}} \cdot \nabla \bar{\mathbf{u}} + \mathbf{f} \times \bar{\mathbf{u}} = -g \frac{\bar{\rho}}{\rho_0} \nabla \eta + \left(\frac{\partial}{\partial z} \nu_e \frac{\partial \mathbf{u}}{\partial z} \right)_{z=\eta}. \quad (4)$$

On a rigid seabed the current velocity vanishes, and (2) is reduced to simply a balance between the horizontal pressure gradient and the vertical momentum diffusion at the bottom, $z = -h$. The bottom pressure gradient obtained from integrating (1) and taking the horizontal derivative is

$$\nabla P|_{z=-h} = g\bar{\rho} \nabla \eta + g \int_{-h}^{\eta} \nabla \rho \, dz. \quad (5)$$

When the density is well mixed vertically in shallow waters, the baroclinic pressure gradient term in (5) may be approximated by

$$g(h + \eta) \nabla \bar{\rho}, \quad (6)$$

and evaluated from the sea surface density field. For now, however, the shallow water baroclinic effect will be assumed to be weak and negligible; the question of baroclinic contribution is addressed later in sections 5 and 6. Thus neglecting the baroclinic pressure gradient, the bottom momentum balance is

$$0 = -g \frac{\bar{\rho}}{\rho_0} \nabla \eta + \left(\frac{\partial}{\partial z} \nu_e \frac{\partial \mathbf{u}}{\partial z} \right)_{z=-h}. \quad (7)$$

The $\nabla \eta$ term, being typically of the order of 10^{-5} or less on the kilometer scale, is seldom measurable and can be eliminated from (4) using (7). The momentum balance (4) becomes

$$\frac{\partial \bar{\mathbf{u}}}{\partial t} + \bar{\mathbf{u}} \cdot \nabla \bar{\mathbf{u}} + \mathbf{f} \times \bar{\mathbf{u}} = \left(\frac{\partial}{\partial z} \nu_e \frac{\partial \mathbf{u}}{\partial z} \right)_{z=\eta} - \left(\frac{\partial}{\partial z} \nu_e \frac{\partial \mathbf{u}}{\partial z} \right)_{z=-h}, \quad (8)$$

which expresses the surface fluid acceleration as the difference between the surface and bottom momentum diffusion.

The surface current shear $\partial \mathbf{u}/\partial z$ changes in response to the local surface wind stress τ_w . The temporal equation governing the surface shear $\bar{\mathbf{s}} = (\partial \mathbf{u}/\partial z)_{z=\eta}$ is

$$\left(\frac{\partial}{\partial t} + \bar{\mathbf{u}} \cdot \nabla \right) \bar{\mathbf{s}} + \bar{\mathbf{s}} \cdot \nabla \bar{\mathbf{u}} - \bar{\mathbf{s}} \nabla \cdot \bar{\mathbf{u}} + \mathbf{f} \times \bar{\mathbf{s}} = \left(\frac{\partial^2}{\partial z^2} \nu_e \frac{\partial \mathbf{u}}{\partial z} \right)_{z=\eta}, \quad (9)$$

which is obtained by differentiating (2) with respect to z and evaluated at the surface. With the vertical shear derivable from wind stress as $\nu_e \bar{\mathbf{s}} = \tau_w$, the left-hand side of (9) can be determined, and hence (9) complements the surface momentum equation (8) by providing additional estimates of vertical diffusion of current shear.

3. Constraints on Velocity Profiles

Equations (8) and (9) allow the viscous diffusion terms to be determined from the measured $\bar{\mathbf{u}}$ and τ_w . In turn, the viscous term can be used to deduce vertical derivatives of the horizontal velocity, with a suitable model for eddy viscosity to be discussed shortly. Vertical derivatives up to the third order are contained in the viscous terms of the foregoing equations. These higher-order vertical derivatives together with the surface shear are indicative of the velocity change with depth adjacent to the surface and bottom boundaries. If the vertical scale of this velocity change is approximately the thickness of the viscous Ekman boundary layer, then in shallow water, where the top and bottom Ekman boundary layers can overlap, the vertical derivative quantities at the boundaries are, in essence, indicative of the velocity variation across the water column. In this case, by invoking the surface derivative quantities as constraints the approximate shape of the subsurface current profile may be inferred.

The crucial assumption here is clearly that the depth variation of the velocity indicated by the surface derivative quantities occurs on a scale comparable to the Ekman boundary layer thickness. One way to insure that this occurs is to obtain the vertical derivative quantities from the diffusion terms in the

context of a depth uniform eddy viscosity model; in such a model all velocity variations with depth are characterized by one vertical scale, namely, the Ekman boundary layer thickness $\delta = \sqrt{2\nu_e/f}$; by contrast, a depth-varying eddy viscosity model based on the turbulence closure theories [e.g., Mellor and Yamada, 1982] supports multiple vertical scales; in particular, the model requires fine scales to exist near boundaries, where vertical shear must rise sharply to compensate for the vanishing eddy viscosity (replaced by molecular viscosity) as the eddy mixing length goes to zero; the high vertical shear and small vertical scale required by such a model near the boundaries clearly cannot characterize the velocity variation across the Ekman boundary layer. Thus, to be consistent with the assumption that underlies the use of the boundary vertical derivative for the velocity inference, the depth uniform eddy viscosity model will be adopted here. At this juncture it is important to note that numerical simulations of shallow water currents carried out with the different types of the eddy viscosity models [Davies and Xing, 1995] have consistently obtained similar current structures. This indicates that as long as a pathway is provided for transferring the viscous stress into the interior, the detail of the viscous transfer near the boundaries is unlikely to be critical. The depth uniform eddy viscosity model provides a simple path for the viscous transfer without considering the detail.

A simple closure relationship such as the one given by Davies and Furnes [1980] may be used to model the depth uniform eddy viscosity. That closure relationship basically assumes that the eddy viscosity is proportional to the mean current speed squared. Here the mean current speed will be taken to be the depth-averaged magnitudes of the inferred velocities \bar{u} and \bar{v} , and hence

$$\nu_e = \frac{k}{\omega} (\bar{u}^2 + \bar{v}^2), \quad (10)$$

where $k = 2 \times 10^{-5}$ is the dimensionless proportionality constant given by Davies and Furnes and ω is the characteristic frequency of the local current; two values of ω are to be tried: $8.42 \times 10^{-5} \text{ s}^{-1}$ and $1.45 \times 10^{-4} \text{ s}^{-1}$, on the basis of the inertial frequency and the semidiurnal tidal frequency, respectively. This parameterization in terms of the mean current speed clearly cannot account for other processes that could affect the eddy viscosity such as surface cooling or wave-induced turbulence; these complications may have to be considered in future improvements of the velocity inference.

Thus, at the sea surface, $z = \eta$, the velocity profiles $\hat{\mathbf{u}}(z) = (\hat{u}, \hat{v})$ are constrained to satisfy the measured sea surface velocities $\bar{\mathbf{u}}$, i.e.,

$$\hat{\mathbf{u}}(z = \eta) = \bar{\mathbf{u}}, \quad (11)$$

as well as, with ν_e from (10), the surface shears from the measured wind stress, i.e.,

$$\left. \frac{\partial \hat{\mathbf{u}}}{\partial z} \right|_{z=\eta} = \bar{\mathbf{s}} = \frac{\boldsymbol{\tau}_w}{\nu_e}, \quad (12)$$

and the higher-order vertical derivatives,

$$\left(\frac{\partial^2 \hat{\mathbf{u}}}{\partial z^2} \right)_{z=\eta} - \left(\frac{\partial^2 \hat{\mathbf{u}}}{\partial z^2} \right)_{z=-h} = \frac{1}{\nu_e} \left(\frac{\partial \bar{\mathbf{u}}}{\partial t} + \bar{\mathbf{u}} \cdot \nabla \bar{\mathbf{u}} + \mathbf{f} \times \bar{\mathbf{u}} \right) \quad (13)$$

$$\left(\frac{\partial^3 \hat{\mathbf{u}}}{\partial z^3} \right)_{z=\eta} = \frac{1}{\nu_e} \left(\frac{\partial \bar{\mathbf{s}}}{\partial t} + \bar{\mathbf{u}} \cdot \nabla \bar{\mathbf{s}} + \bar{\mathbf{s}} \cdot \nabla \bar{\mathbf{u}} - \bar{\mathbf{s}} \nabla \cdot \bar{\mathbf{u}} + \mathbf{f} \times \bar{\mathbf{s}} \right) \quad (14)$$

from (8) and (9), respectively. At the seabed, $z = -h$, the no-slip condition can be enforced:

$$\hat{\mathbf{u}}(z = -h) = 0. \quad (15)$$

The boundary conditions (11)–(15) certainly do not represent the complete set of constraints. Differentiating the governing equation repeatedly with respect to z can produce still higher order vertical derivatives, which are applicable to the surface as additional constraints. In practice, however, derivatives of order higher than that of (14) are unlikely to be obtained reliably because of the increasing differentiation errors, nor in the present case is there a compelling reason to obtain higher-order constraints since the scale of the flow being considered here is limited to $\sim \delta$, the Ekman boundary layer thickness.

Because (11)–(15) are intended for inferring current structure having a vertical scale of δ , the maximum water depth to which (11)–(15) are applicable will be taken to be the combined height of the surface and bottom Ekman boundary layers, or $\sim 2\delta$. Still another factor that must be considered is the timescale of vertical viscous diffusion, $t_d \sim \delta^2/(4\nu_e)$, versus the timescale of the current, t_c . For the surface and bottom Ekman boundary layers to merge t_c has to be greater than t_d . Being predominantly driven by tides and winds, coastal currents tend to evolve on the timescale $t_c \sim \text{O}(\text{day})$ of the forcing functions. This timescale is long compared to $t_d \sim \text{O}(\text{hour})$ for a moderate eddy viscosity value, say, $\nu_e \sim 0.01 \text{ m}^2 \text{ s}^{-1}$ and a δ in the range of 10–30 m. Therefore it should be possible for the viscous influence to be established across the water depth within the timescale of the current motion (\geq tidal period) of interest to this study.

4. Modal Representation

To infer current velocity as a function of depth from the boundary conditions (11)–(15), it can be advantageous to adopt a basis function representation, i.e., to express the velocity, $\hat{\mathbf{u}}(z)$, to be inferred as a linear combination of orthogonal basis functions,

$$\hat{\mathbf{u}}(\mathbf{x}, z, t) = \sum_{i=0}^N \mathbf{c}_i(\mathbf{x}, t) F_i(z), \quad (16)$$

where $F_i(z)$ is the basis function and \mathbf{c}_i is the weight. With $\hat{\mathbf{u}}(z)$ in this form the problem of inferring velocity is then reduced to finding the values of \mathbf{c}_i such that $\hat{\mathbf{u}}(z)$ and its derivatives evaluated at the boundaries satisfy the constraints (11)–(15). However, since there are only five boundary conditions, there can only be five weights that determine $\hat{\mathbf{u}}(z)$ uniquely, and the linear sum (16) here is necessarily limited to $N = 4$. For frictionally dominated flow an effective approximation of $\hat{\mathbf{u}}(z)$ with five weights may be achieved with the Chebyshev polynomial basis functions, which have been widely used in numerical simulations of viscous shear flow for their ability to capture efficiently velocity change at the viscous boundaries [Canuto et al., 1988]. (Other basis function sets are also possible [see, e.g., Davies, 1982].) Figure 1 shows the first

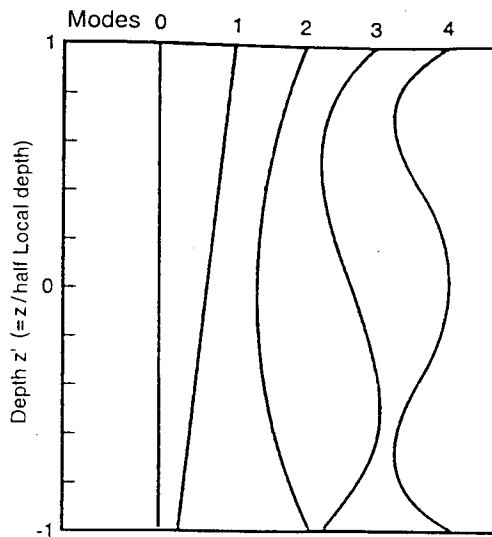


Figure 1. The first five Chebyshev polynomial basis functions.

five modes of the Chebyshev polynomials, where the depth $-h < z < \eta$ has been converted to the standard dimensionless interval $-1 < z' < 1$ spanned by the polynomials. Each mode has one more oscillation than the previous mode; it is seldom that a fully evolved viscous flow exhibits variation greater than that in mode 4, in particular, across the depth of the Ekman boundary layer. Regardless, it will be possible to verify the adequacy of the approximation a posteriori as the weights obtained should decrease in magnitude with increasing order of F_i if the finite sum (16) converges for $N = 4$.

4.1. Solution

To use the Chebyshev polynomials as the basis functions, it is necessary to scale the depth range $-h \leq z \leq \eta$ to the dimensionless range $-1 \leq z' \leq 1$ for which the polynomials are defined. Thus, with $z' = 1 + 2(z - \eta)/H$, where $H = h + \eta$ and where $F_i(z')$ denotes the Chebyshev polynomial of mode i , (16) in component form can be written

$$\hat{u}(x, z', t) = \sum_{i=0}^4 \alpha_i(x, t) F_i(z') = \mathbf{A} \cdot \mathbf{F}^T \quad (17)$$

$$\hat{v}(x, z', t) = \sum_{i=0}^4 \beta_i(x, t) F_i(z') = \mathbf{B} \cdot \mathbf{F}^T, \quad (18)$$

where \mathbf{A} and \mathbf{B} are row vectors containing the weights α_i and β_i , respectively, and \mathbf{F} is the row vector of F_i .

In the boundary conditions (12)–(14) the vertical derivatives are related to the derivatives with respect to z' by

$$\left. \frac{\partial^n \hat{u}}{\partial z'^n} \right|_{z'=1 \text{ or } -1} = \left(\frac{H}{2} \right)^n \left. \frac{\partial^n \hat{u}}{\partial z^n} \right|_{z=\eta \text{ or } -h}, \quad (19)$$

where $n = 1, 2$, or 3 . Let $\mathbf{G} = \{G_{ij}\}$ be a 5 by 5 matrix defined by

$$G_{1,j} = F_j|_{z'=1},$$

$$G_{2,j} = \left. \frac{\partial F_j}{\partial z} \right|_{z'=1},$$

$$G_{3,j} = \left. \frac{\partial^2 F_j}{\partial z^2} \right|_{z'=1} - \left. \frac{\partial^2 F_j}{\partial z^2} \right|_{z'=-1},$$

$$G_{4,j} = \left. \frac{\partial^3 F_j}{\partial z^3} \right|_{z'=1},$$

$$G_{5,j} = F_j|_{z'=-1}$$

with $j = (1, 2, \dots, 5)$. Substituting (17) and (18) into the left-hand side of the boundary conditions (11)–(15) and making use of (19), five equations relating five unknown weights for each \hat{u} and \hat{v} component are obtained and in matrix form are

$$\mathbf{G} \cdot \mathbf{A} = \mathbf{U} \quad (20a)$$

$$\mathbf{G} \cdot \mathbf{B} = \mathbf{V}, \quad (20b)$$

where \mathbf{U} and \mathbf{V} are column vectors containing the values given by the right-hand side of (11)–(15) multiplied by appropriate factors of $H/2$.

Equations (20a) and (20b) are a linear system only if ν_e is known a priori since both \mathbf{U} and \mathbf{V} are functions of $1/\nu_e$ and ν_e , in turn, is a function of the unknowns \mathbf{A} and \mathbf{B} . It is difficult to solve the nonlinear system (20a), (20b), and (10) simultaneously for \mathbf{A} and \mathbf{B} . However, an iterative procedure may be adopted as follows: First, an initial guess of ν_e is made using the measured surface velocity \bar{u} in (10). Next, this ν_e is used in \mathbf{U} and \mathbf{V} to render (20a) and (20b) a linear system. \mathbf{A} and \mathbf{B} obtained by inverting this linear system are then substituted into (16) to make a first estimate of \hat{u} . From this first \hat{u} estimate, \bar{u} and \bar{v} are calculated and used in (10) to update ν_e . The same procedure applied again using the updated ν_e yields the second estimate of \hat{u} . In this manner of successive correction, \hat{u} and ν_e are to be iterated. Since ν_e is a scalar, the convergence of the iteration may be determined by a preset accuracy for ν_e . The convergence is generally assured with a reasonable starting value for ν_e such as one based on \bar{u} because of the inverse dependence of the boundary values \mathbf{U} and \mathbf{V} on ν_e . This inverse dependence has the effect that an overestimation of \bar{u} increases ν_e and reduces \mathbf{U} and \mathbf{V} so that on the next iteration, \bar{u} is decreased. The opposite happens for underestimated \bar{u} . Hence there is a tendency for this negative feedback between ν_e and \mathbf{U} and \mathbf{V} to steer the solution toward convergence. In passing it may be noted that although, in principle, more than five modes can be included in (16), and the resulting underdetermined system (20) can be solved using the method of single-value decomposition, this does not necessarily yield a better result as the additional higher modes can weaken the constraining effect of low-order derivative boundary conditions.

4.2. Effect of Boundary Error

To assess the effect of the errors in the boundary values \mathbf{U} and \mathbf{V} on the subsurface \hat{u} and \hat{v} estimates, ν_e can be assumed to be given. Let $\mathbf{E} = \{E_j\}$ be the error vector in \mathbf{U} and \mathbf{V} , where $j = 1$ refers to the surface velocity, $j = 2$ refers to the shear, $j = 3$ refers to the curvature, $j = 4$ refers to the third z derivative, and $j = 5$ refers to the bottom velocity, which is taken here to be error free. Since for a given ν_e , (20a) and

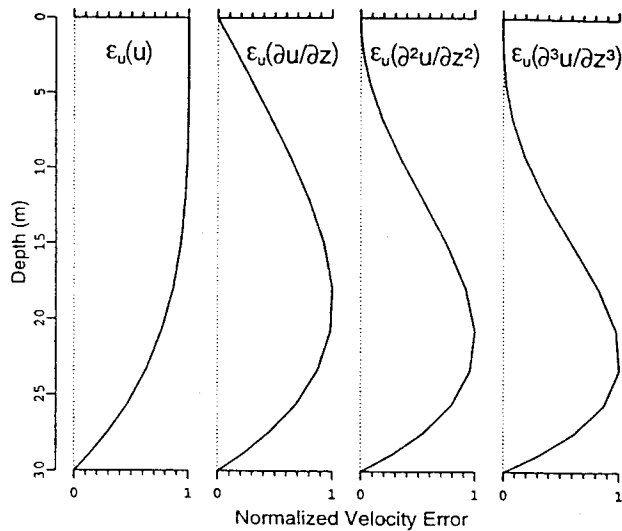


Figure 2. Normalized velocity error ϵ_u as a function of depth. Each curve represents the error from the individual surface source in parentheses.

(20b) are a linear system, the error vector $\mathbf{e} = \{e_j\}$ for the modal coefficients are readily obtained:

$$\mathbf{e} = \mathbf{G}^{-1} \cdot \mathbf{E}. \quad (21)$$

The error in the subsurface \hat{u} velocity estimate is (same for \hat{v})

$$\epsilon_u = \mathbf{e} \cdot \mathbf{F}^T. \quad (22)$$

In Figure 2 the error profile ϵ_u versus depth is shown separately for each input surface error. The error range has been normalized to unity. It is seen that the \hat{u} error is largest toward the bottom for surface derivative errors, while the error in surface velocity propagates mostly undiminished toward the bottom.

5. An Oceanic Application

5.1. Field Data

The inference of subsurface current velocity will be demonstrated here with data obtained during the High-Resolution Remote Sensing Experiment-2 (HIRES-2), which was conducted on the continental shelf area off the coast of Cape Hatteras between June 10 and June 26, 1993 (Figure 3). The experiment, jointly sponsored by the Office of Naval Research and the Naval Research Laboratory, was designed to obtain high-resolution radar images of the sea surface by using airborne microwave band radar and, simultaneously, to collect in situ hydrographic and current data from ships and surface velocity data from the shore-based HF radar to assist in the interpretation of the imagery. However, the deployment of these different measurement platforms also provided an opportunity to make comprehensive observations of the circulation in the region. In particular, the observation identified recurring intrusion of energetic flows onto the shelf, apparently mostly of Gulf Stream origin. The intruding flow is directed northeastward, while its axis translates progressively northwestward or inshore to as far as midshelf. The intrusion, recurring roughly on the timescale of the Gulf Stream meander or about 3–5 days, dominates the circulation in the region

despite the fact that tidal and wind-driven currents are also present. For a description and analysis of the current variability and dynamics in the area as well as the modeling of the intrusion event the reader may refer to Mied *et al.* [1996], Marmorino *et al.* [1998], Jansen *et al.* [1998], and Shen *et al.* [2000].

The surface current velocity during the experiment was measured using a commercially available HF OSCR system, which resolved the current at ~ 1.2 km scale and 20 min intervals over a 30×40 km area. Figure 3 shows the radar sites and the area measured, where each dot marks the position of the cell at which a current vector averaged over ~ 2.5 – 5.6 km² is obtained as a function of time; the reader is referred to Shay *et al.* [1995] for the detailed operation of the system during the experiment. However, the reliable wind data were obtained only at the disc buoy Dw. The surface velocity data to be used for inferring the subsurface velocity are limited to those obtained in the vicinity of Dw and during the period between 1400 and 1600 UT on June 23, when the ship was in the same area making in situ current measurements with the acoustic Doppler current profiler (ADCP). This period is also of interest in that it is coincident with the end of an intrusion event.

The shipboard ADCP survey was made within the outlined area in Figure 3. An enlarged view of the area and the current measured by OSCR is shown in Figures 4 and 5 for 1400 and 1600 UT, respectively. Diamond symbols mark the ship positions at which in situ ADCP current profiles (5 min averaged) were obtained; the solid circles mark the OSCR cells with surface velocity vectors that are used for inferring the subsurface current. For the purpose of comparing the current profiles inferred from OSCR to those measured by ADCP, OSCR and ADCP velocity data closest in space and time are grouped and marked as indicated by P1–P5. For P1, P2, and P5, four OSCR

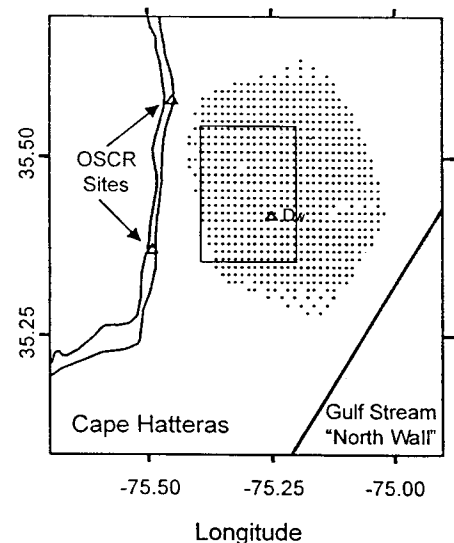


Figure 3. The experimental area. Surface current velocity vectors are measured by the OSCR HF radar system in the dotted area, where each dot represents a location at which the velocity vector is obtained as a function of time. The locations of the two HF radars are indicated by the small triangle along the shoreline. The triangle in the dotted area marks the location of the disc buoy Dw at which the near-surface wind is measured. The ship ADCP survey is made within the outlined area. The mean inshore edge of the Gulf Stream is also indicated.

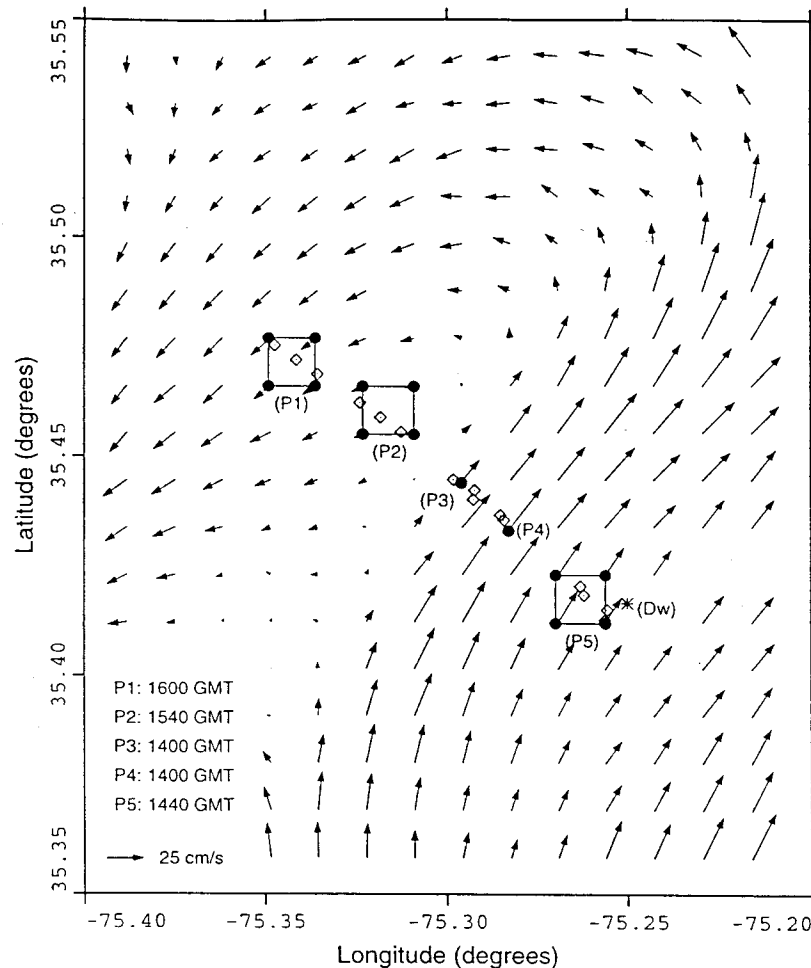


Figure 4. Sea surface current vectors measured by OSCAR at 1400 UT, June 23, 1993. The velocity vectors at the locations marked by the solid circles are compared to the near-surface current velocity measured at ~ 2 m depth by the ship-towed ADCP at the locations marked by the diamonds. The measurements closest in space and time are grouped as P1–P5.

cells compose a group, while for P3 and P4, only one OSCAR cell is in each group. Assigned to each group is a mean time taken at the midpoint between the first and last ADCP measurements made within a given group. All OSCAR velocity vectors shown in Figures 4 and 5 have been smoothed with a 6 hour low-pass filter.

The current vectors at 1400 UT (Figure 4) show an elongated cyclonic surface flow oriented in the NE–SW direction. In the offshore direction the stronger NE flow is the remnant of the Gulf Stream intrusion that occurred a day earlier [Marmorino *et al.*, 1998]. This remnant flow is seen subsequently weakened and turned clockwise in the current vector map at 1600 UT (Figure 5). In contrast, the inshore SW flow is strengthened and turned counterclockwise. These changes are apparently the result of the surface wind stress, which acts in the southwestward direction during this period. The dominance of the northeasterly wind is evident in the wind velocity vector plot (dotted arrows) in Figure 6, where the wind vector measured at Dw at the time indicated is placed tail first at the center of each group. Since the wind was measured only at Dw, the wind vector is assumed to be valid at all five locations for use in the subsurface velocity inference.

Shown in Figure 6 with the wind vectors are the surface

current velocity vectors from OSCAR (dashed arrows); at P1, P2, and P5 the four-point-averaged velocity vectors are plotted. For comparison, the in situ current velocity vectors at ~ 2 m depth, the shallowest depth measured by ADCP, are averaged within each group and plotted as well (solid arrows). It is evident that a large discrepancy exists between the OSCAR and ADCP velocity vectors despite their having been obtained from measurements located closely in space and time. Chapman *et al.* [1997] have made a comparison of all closely located OSCAR and ADCP velocity data obtained in HIRIS-2. They obtained rms differences of about $15\text{--}16\text{ cm s}^{-1}$ for each of the u and v velocity components. The current vector differences shown in Figure 6 are consistent with this rms value. Their analysis deduces a measurement uncertainty of $\sim 7\text{--}8\text{ cm s}^{-1}$ for the OSCAR system and attributes the remaining differences between the OSCAR and ADCP data to differences in instrument resolution, small-scale current variability, and the noise in the ADCP system. The instrument resolution is believed to be the more serious in that the ADCP system makes local measurement of the current velocity from a moving ship while the OSCAR system measures surface velocities averaged over a $2.5\text{--}5.6\text{ km}^2$ area, as noted earlier. In an area of rapidly changing current velocities this resolution difference could give rise

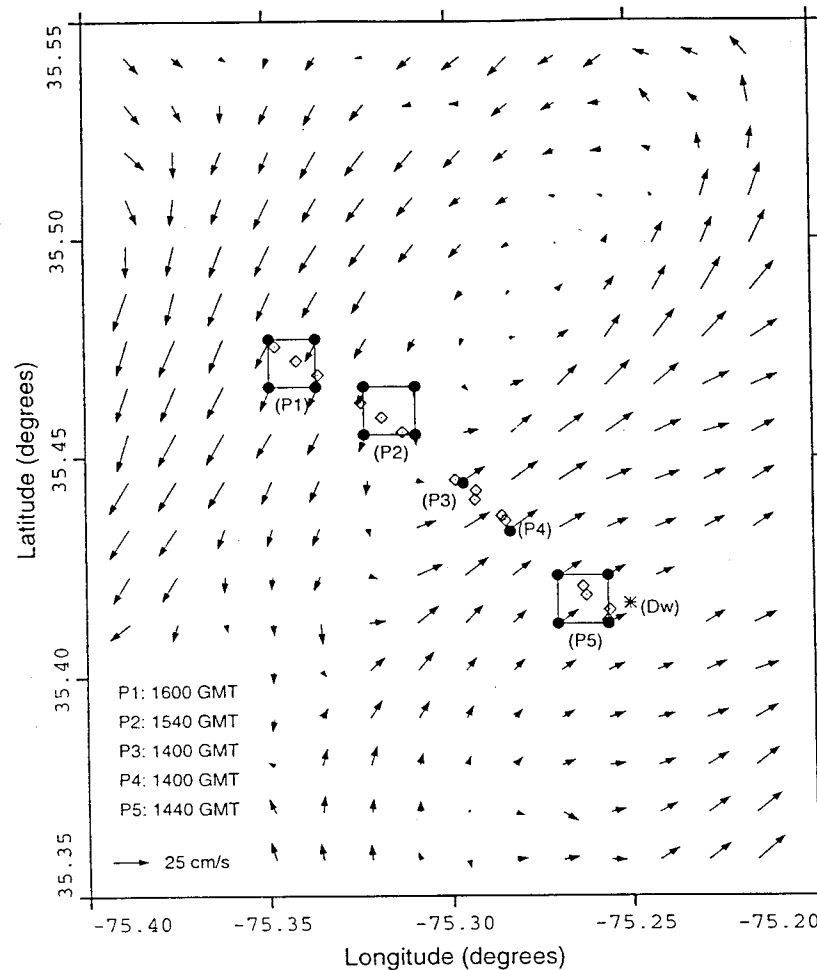


Figure 5. Same as Figure 4 but at 1600 UT, June 23, 1993.

to large discrepancies. This is apparently the case at P3, which is situated in a region of large velocity gradient (see Figure 4).

5.2. Current Profile Comparisons and Sensitivity Tests

For inferring the subsurface velocity the OSCR surface velocity vectors shown in Figure 6 are used in (11) as one of the boundary conditions, and the wind velocity vector is converted to surface shear stress using the bulk formula $\tau_w = 0.00123 C_d W^2$, where C_d is the wind speed-dependent drag coefficient and W is the wind speed at 10 m height. The computed shear stress is then used in the boundary condition (12). The calculation of the right-hand side terms for the boundary condition (13) uses the centered finite differencing scheme for both the time and spatial derivatives. The same scheme is applied to the calculation of the time derivative terms for (14), but the nonlinear spatial derivative terms are not evaluated in the absence of spatial wind data. The surface velocity data and wind data used here have all been preprocessed with a 6 hour low-pass filter to retain only lower-frequency motions including the dominant semidiurnal tidal constituent.

The downward projection of the OSCR data using the boundary conditions and the iterative solution procedure given in section 4 yields the current velocity profiles (solid curves) shown in Figure 7. The profiles are obtained with ω set to the inertial frequency in the eddy viscosity relation (10). The same

could also have been shown by using the semidiurnal tidal frequency for ω . The results are relatively insensitive to ω , as will be seen shortly. For comparison, also shown in Figure 7 are the in situ current profiles measured by ADCP (light curves; the large fluctuations at bottom are due to ground interference and are to be ignored). Additionally, to see how the uncertainty in the surface velocity data may affect the inference, plotted as well are the velocity profiles (dashed curves) calculated by the same procedure but replacing the surface velocities from OSCR with near-surface velocities from ADCP in the boundary condition (11) while keeping the other four boundary conditions unchanged.

It can be seen that the two sets of profiles inferred separately from the OSCR data and the near-surface ADCP data are qualitatively similar. The large velocity differences between the two sets of profiles near the surface simply decrease with increasing depth, a trend consistent with the error curve related to the surface velocity uncertainty $\epsilon_u(u)$ shown in Figure 2, even though their eddy viscosity magnitudes, determined as a part of the calculation, are quite different (Table 1). Both sets of profiles inferred from the surface data deviate noticeably from the in situ current profiles measured by ADCP. Nevertheless, both are able to capture the general structure of the v velocity component at P5 to the S-shaped profile for the u

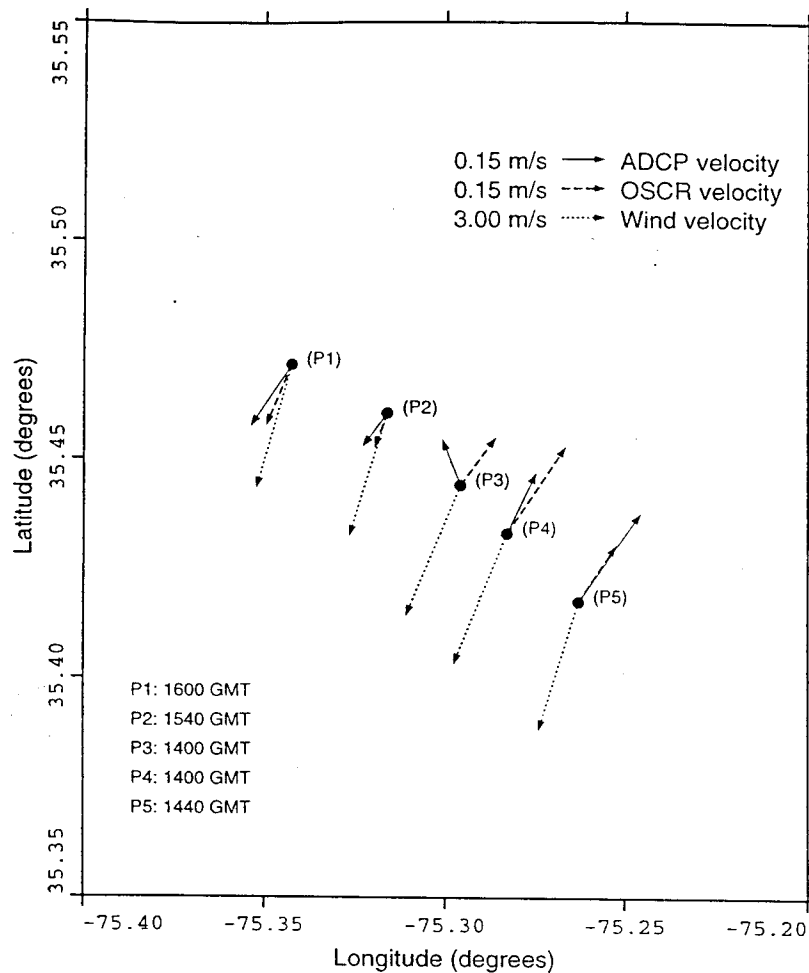


Figure 6. Comparison between OSCR surface velocity vectors, the ADCP near-surface velocity vectors at ~2 m depth, and the wind velocity vectors at 10 m height. The OSCR surface velocity vector at P1, P2, and P5 is the average of four vectors.

velocity component at P1. The agreement is significantly improved for the profiles inferred from the near-surface ADCP data and is nearly exact for the v velocity component at P4 and P5. The question may arise as to whether the result is significantly better than a straight-line profile that starts from zero at bottom and increases linearly to the surface velocity value without the added surface dynamical constraints. The rms values of velocity magnitude differences calculated with respect to the ADCP for the straight-line profiles at all five locations are greater than those calculated for the profiles inferred with the present method; in particular, the differences are greater by a factor of 2 at P2 and P5. Hence the inclusion of surface dynamic constraints is, in fact, helpful.

The deviation between the inferred profiles with surface dynamic constraints and those measured in situ by ADCP can be the result of a number of factors, however, in addition to the inherent noise in the surface OSCR data. One is the instrument resolution difference noted earlier between the OSCR and ADCP systems. The others are (1) the choice of characteristic frequency for calculation of the eddy viscosity in (10), (2) the truncated five-mode approximation of the profiles, (3) the neglect of the baroclinic pressure effect, and (4) the assumption of uniform wind. The alternate choice of using the semidiurnal tidal frequency as the characteristic frequency for

the eddy viscosity calculation does not significantly affect the results shown in Figure 7, which are obtained with the smaller inertial frequency. This is so despite the almost factor of two difference between the two frequencies. With the higher tidal frequency (lower viscosity) the inferred profiles differ from those shown in Figure 7 in only having a somewhat larger velocity amplitude by about $\leq 5 \text{ cm s}^{-1}$. This amplitude increase does not necessarily improve the agreement with the measurement, however. An example is shown in Figure 8, where the u component profile for the lower-viscosity case (dashed curve) deviates less from the measured while at the same time the deviation in the v component is increased. The five-mode approximation can be inadequate if the finite sum (16) fails to converge. The weights obtained for all five cases P1–P5 are found to decrease with increasing order of Chebyshev polynomials. The decrease is a decade or more from the third to the fifth mode, indicative of convergence.

The neglect of the baroclinic pressure gradient affects the accuracy of the boundary condition (13). This pressure gradient effect was neglected when the difference was taken between (4) and (7). The inaccuracy of (13) also arises from estimating the terms in the equation using the OSCR data. Particularly large errors can arise in the nonlinear term estimate as unresolved spatial fluctuations (less than the kilometer

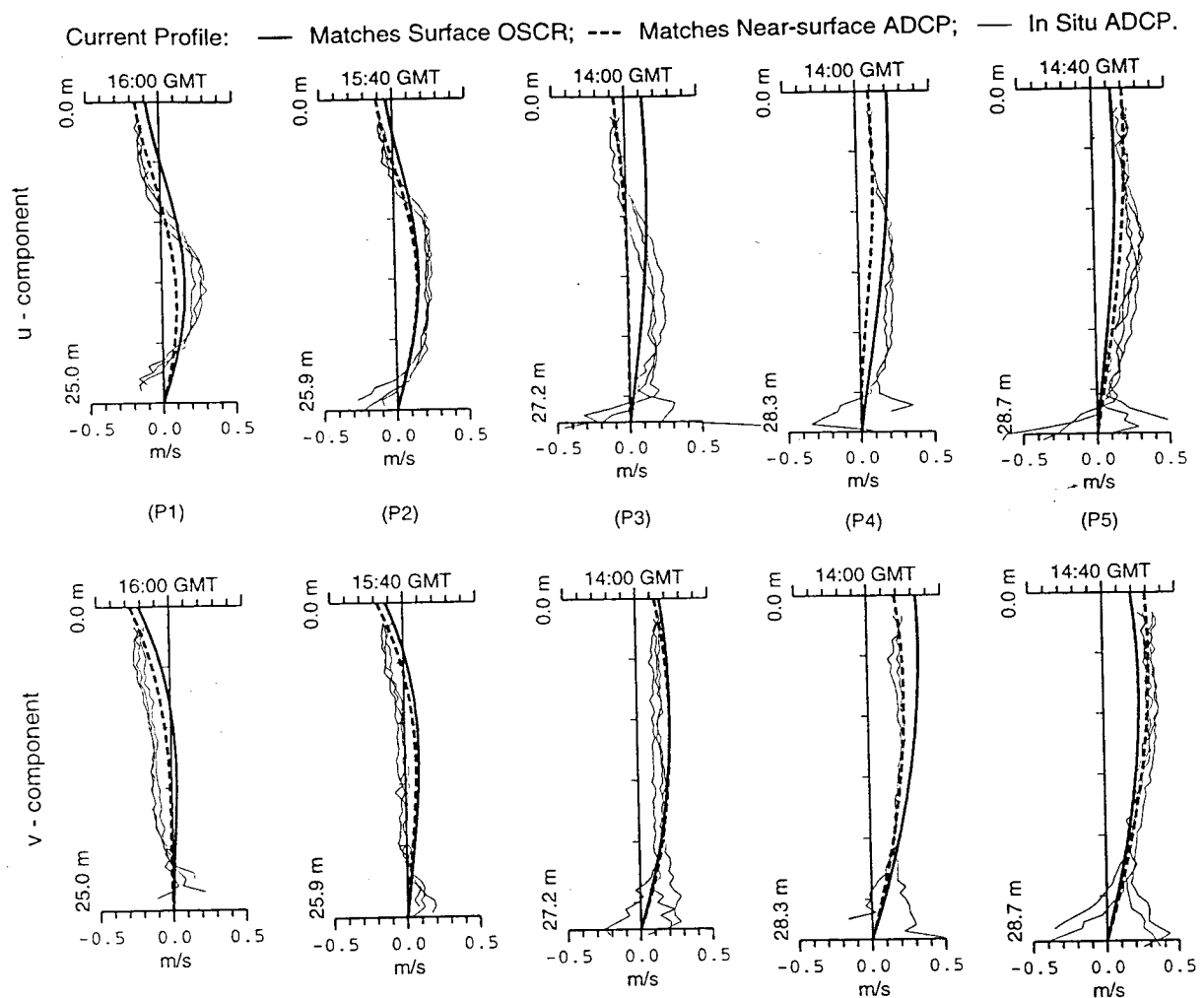


Figure 7. Comparison of the current profiles inferred from OSCR data and near-surface ADCP data to the current profiles measured in situ.

scale) of $O(10 \text{ cm s}^{-1})$ are still present in the OSCR data despite the temporal smoothing of the data. This noise multiplied by the spatial finite differencing error $\sim (10 \text{ cm s}^{-1})/1.2 \text{ km}$ results in a nonlinear term error of $O(10^{-5} \text{ m s}^{-2})$. The uncertainty due to the neglect of the baroclinic pressure gradient (6) is estimated to be $(gh/\rho_0)(\Delta\rho/\Delta L) \approx 1 \times 10^{-5} \text{ m s}^{-2}$ based on $h \approx 25 \text{ m}$ and the shipboard measurement of the surface $\Delta\rho \approx 4 \times 10^{-4} \text{ g cm}^{-3}$ over a distance $\Delta L \approx 10 \text{ km}$, assuming that this density difference is the same for the whole water column. Thus the contribution to the uncertainty in the boundary condition (13) from the baroclinic pressure gradient and nonlinear terms may be as large as $2 \times 10^{-5} \text{ m s}^{-2}$. The wind stress magnitude and direction can be in error since the wind measured at a single disc buoy is assumed to be applica-

ble to all five locations. The wind stress error affects the boundary conditions (12) and (14). The neglect of nonlinear terms in (14) due to the absence of spatial data additionally affects the accuracy of (14). The wind magnitude and direction at Dw varied at most by about 10% and 10° , respectively, during the 2 hour period. Here it will be simply assumed that the spatial errors in the wind stress are no more than twice as large, i.e., 20% and 20° in magnitude and direction; at the same time the nonlinear term error in (14) may be taken to be $(|\tau_w|/\nu_e)(\Delta|u|/\Delta L) \approx 5 \times 10^{-7} \text{ s}^{-2}$, for $|\tau_w| \sim 10^{-5} \text{ m}^2 \text{ s}^{-2}$, $\nu_e \sim 0.01 \text{ m}^2 \text{ s}^{-1}$, $\Delta|u| \sim 0.1 \text{ m s}^{-1}$, and $\Delta L \sim 1 \text{ km}$.

The sensitivity of the result to the uncertainties in the boundary conditions (12)–(14) is checked by perturbing the boundary values one at a time with the errors estimated above.

Table 1. The ν_e and δ for $\omega = f = 8.42 \times 10^{-5} \text{ s}^{-1}$ for OSCR (ADCP)

	P1	P2	P3	P4	P5
$\nu_e, \text{m}^2 \text{s}^{-1}$	4.12×10^{-3} (4.34×10^{-3})	4.42×10^{-3} (3.92×10^{-3})	1.27×10^{-2} (9.06×10^{-3})	2.33×10^{-2} (1.21×10^{-2})	1.36×10^{-2} (2.87×10^{-2})
δ, m	9.9 (10.2)	10.2 (9.6)	17.4 (14.7)	23.5 (17.0)	18.0 (26.1)

— Matches OSCR, ω_i
 --- Matches OSCR, ω_t
 — In Situ ADCP

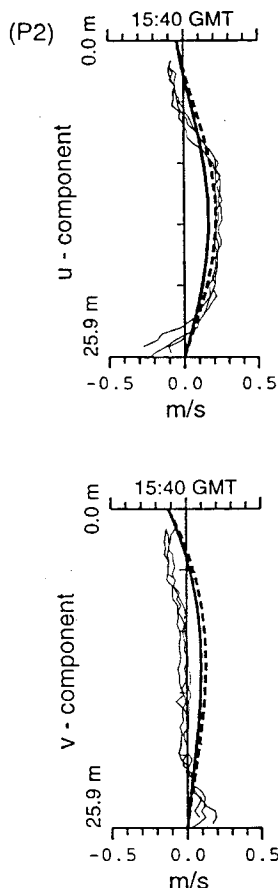


Figure 8. Comparison of the current profiles inferred from OSCR data based on two different characteristic frequencies for the eddy viscosity magnitude. The two frequencies are ω_i and ω_t , the inertial and the semidiurnal tidal frequencies, respectively.

In these tests the near-surface velocity measured by ADCP is used as the velocity boundary condition (11) and is assumed to be error free. The tests show that the inference of subsurface velocity is least affected by the error in boundary condition (14) for the third vertical derivative; the error alters the amplitude of the inferred velocity by only a few cm s^{-1} . The inference is somewhat more affected by the error in the boundary condition (13) on the second vertical derivative; the error alters the velocity amplitude by $\sim 5 \text{ cm s}^{-1}$ in some cases but not the overall shape of the profile. The wind stress error in the vertical shear boundary condition (12) has a still larger effect on the velocity amplitude, causing change as much as $\sim 10 \text{ cm s}^{-1}$, mostly from the wind stress direction error, however; again, the overall shape of the profile is little affected. The

--- Matches near-surface ADCP
 Modified
 — In Situ ADCP

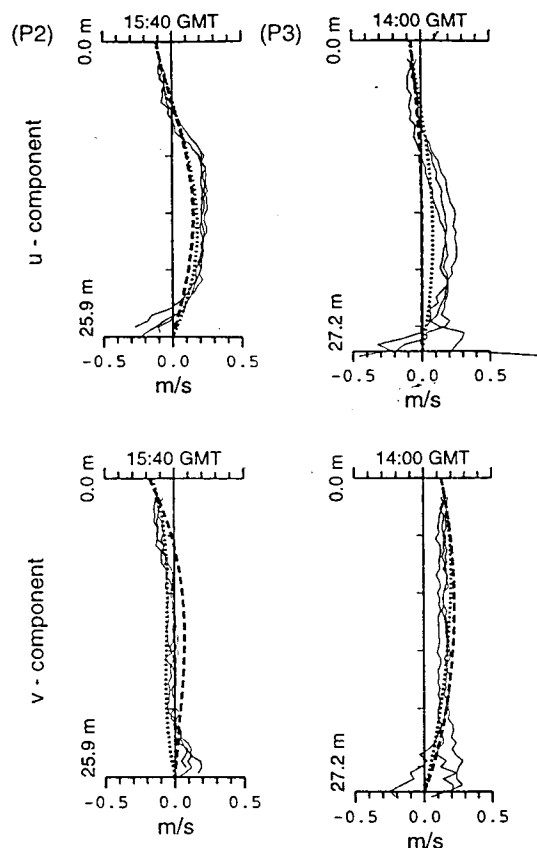


Figure 9. Comparison of the current profiles inferred from the near-surface ADCP data with and without modification to the surface boundary conditions based on presumed measurement uncertainties.

change of inferred velocity amplitude caused by the error in each of the boundary conditions examined here is clearly far from sufficient to explain the deviations shown in Figure 7 between the inferred (dashed curves, in the present case) and the measured (light solid curve) current profiles. However, the velocity change due to the combined errors in (12)–(14) is significantly larger. This is illustrated in Figure 9 for the current profiles at P2 and P3. The second subsurface velocity estimates (dotted curve) are obtained by changing the wind direction at P2 and P3 by 18° and 14° to 235° by adding to and subtracting from the x and y components of (13) an uncertainty of $2 \times 10^{-5} \text{ m s}^{-2}$ and by adding to and subtracting from the x and y components of (14) an uncertainty of $5 \times 10^{-7} \text{ s}^{-2}$. This second estimate obtained from the simultaneous perturbation of the boundary values with these presumed errors can be seen in Figure 9 to account for a significant fraction of the

Table 2. Sea Surface Height Gradients

	P1	P2	P3	P4	P5
$\partial \eta / \partial x$	-5.4×10^{-7}	2.4×10^{-7}	2.6×10^{-7}	1.2×10^{-6}	1.2×10^{-6}
$\partial \eta / \partial y$	-7.7×10^{-7}	4.6×10^{-7}	2.8×10^{-6}	-2.6×10^{-6}	-1.1×10^{-6}

Table 3a. Surface u -Momentum Balance^a

	$\partial u / \partial t$	$+u \cdot \nabla$	$-fv =$	$-g \partial \eta / \partial x$	$+v_e \partial^2 u / \partial z^2$
P1	4.27×10^{-6}	3.34×10^{-6}	1.76×10^{-5}	5.3×10^{-6}	1.99×10^{-5}
P5	-5.54×10^{-7}	-4.30×10^{-7}	-1.64×10^{-5}	-1.16×10^{-5}	-5.8×10^{-6}

^aIn m s^{-2} .

deviation between the previously inferred and measured profiles.

The relative insensitivity of the inference to the uncertainties in the derivative boundary conditions (12)–(14) can be attributed to the inverse dependence of the vertical derivatives on the velocity-dependent eddy viscosity. Since the sources of the boundary derivative errors are actually the wind stress, the momentum, and the shear terms on the right-hand side of (12)–(14), the fact that these quantities are divided by the eddy viscosity to yield the vertical derivatives means that the actual boundary derivative errors are always reduced as the eddy viscosity magnitude is increased, in proportion to the square of the error in the inferred velocity via (10). The decreased boundary derivative errors in turn mean a smaller error in the inferred velocity. In this sense the present inference procedure may be viewed as robust.

5.3. Surface Momentum Balance

The inferred subsurface current velocity permits bottom momentum diffusion in (7) to be calculated, from which the unknown sea surface height gradients are then also determined. At this point all the terms in the momentum balance (4) are known, including the surface viscous term calculable from the inferred velocity profile and eddy viscosity, and the resulting balance is exact, except for round off errors. The two terms, sea surface height gradient and viscous diffusion, in (4) are difficult to obtain by measurements. Their determination as a part of the surface-to-subsurface velocity projection is potentially useful for diagnostic analysis. In Table 2 the values of the two horizontal components of the gradients are listed for the five sites, and in Tables 3a and 3b the values of the terms in the surface momentum equations for u and v , are listed for inshore P1 and offshore P5 sites, respectively.

The east-west component $\partial \eta / \partial x$ shows a rising sea surface level in the offshore direction. The north-south component $\partial \eta / \partial y$ shows two reversals of the sea surface slope from offshore to inshore. At the inshore location P1 the momentum balance shows that the Coriolis force balances mostly u momentum diffusion and convective acceleration in the east-west direction and balances the surface pressure gradient in the north-south direction. The east-west component of local current acceleration $\partial u / \partial t$ is primarily driven by the pressure gradient, while the north-south component $\partial v / \partial t$ is driven by surface momentum diffusion resulting from the wind stress forcing, which is directed mostly southward at this time. At the offshore location P5, where the largest current speed occurs,

there is an approximate balance between the Coriolis force and the pressure gradient in both horizontal directions. The local current acceleration in both directions is negative, indicating the current is slowing down. This deceleration is consistent with the wind forcing at this time, which is opposite to the flow direction, as shown in Figure 6. The negative values of both u and v momentum diffusion reflect the transmission of this wind stress into the water.

6. Conclusions

An inference approach that obtains subsurface current structure from the surface current data in shallow water, defined by depth $\leq 2\delta$, i.e., not exceeding the combined height of surface and bottom Ekman boundary layers, has been described in this paper. The approach relies on δ 's being the only vertical scale that characterizes the velocity change with depth within the overlapping viscous Ekman boundary layers. This allows the current profile to be constrained by boundary vertical derivatives derivable from surface viscous momentum and shear diffusion. The assumption of a single vertical scale, however, has necessitated the use of a depth uniform eddy viscosity model. A simple closure relationship is chosen that relates the eddy viscosity magnitude to the depth-averaged current speed. With this relationship the eddy viscosity magnitude is determined in a consistent manner with the inference of the subsurface current structure.

It has been possible to apply the present approach to infer subsurface current structure from the surface current measured by the OSCAR radar system in HIRE-2 conducted on the shallow continental shelf off Cape Hatteras. The comparison of the inferred current structure to that measured in situ by the shipboard ADCP has been made difficult by the measurement noises in both the OSCAR and ADCP systems as well as by their very different spatial resolutions: The OSCAR resolves the surface current at kilometer scale, whereas ADCPs make a measurement of the current profile locally. Nevertheless, the inference has been able to capture qualitatively the structure of the measured current, and the result has been improved somewhat with the use of the near-surface velocity measured by ADCP as an alternative boundary condition for the inference. Because the local sea surface height slope and eddy viscosity are determined as a part of the inference of the subsurface velocity, it has also been possible to evaluate the wind stress input and the pressure gradient forcing to identify the likely cause of the surface current change in the experimental area.

Table 3b. Surface v -Momentum Balance^a

	$\partial v / \partial t$	$+u \cdot \nabla$	$+fu =$	$-g \partial \eta / \partial y$	$+v_e \partial^2 v / \partial z^2$
P1	-1.48×10^{-5}	1.05×10^{-6}	-7.45×10^{-6}	-7.5×10^{-6}	-1.36×10^{-5}
P5	-2.09×10^{-5}	-1.80×10^{-6}	1.09×10^{-5}	1.06×10^{-5}	-2.24×10^{-5}

^aIn m s^{-2} .

Present inference is relatively insensitive to uncertainties in the boundary values of the vertical derivatives (12)–(14), which have been used to constrain the current profile. Within the range of the estimated uncertainties the inferred current profile is found to change relatively little in shape, and the inferred current velocity varies only moderately $< \sim 10 \text{ cm s}^{-1}$. The first derivative boundary error (12) related to the uncertainty in the wind direction has the largest effect, followed by the second derivative boundary error (13), and, last, the third derivative boundary error (14). The relative insensitivity to the errors in the input boundary values is attributed to the interdependence between the eddy viscosity, the inferred mean current speed, and the values of the vertical derivatives as discussed in section 5.

The baroclinic pressure gradient effect is not considered in this study. However, if the water is well mixed vertically and the surface temperature and salinity are known, it should be possible to include this effect in the consideration in an approximate manner like (6). The inclusion of the baroclinic pressure effect will require additional sea surface data on temperature and salinity. The sea surface temperature field is measurable synoptically with remote sensors such as airborne radiometer. The synoptic measurement of the sea surface salinity has become feasible recently with the advent of the airborne salinometer [see, e.g., Miller *et al.*, 1998].

The current velocity profiles obtained from the inference in this study necessarily satisfy the governing momentum equations at the sea surface since the governing equations have been used as the dynamic boundary conditions for the inference. It would be desirable to obtain current profiles that satisfy the governing equations at all depths. This possibility is presently under investigation.

Acknowledgments. The authors thank Clifford Trump for providing the ADCP data and Lynn Shay and Hans Graber for providing the OSCR data. The authors have also benefited from discussions with Richard Mied. This work is a contribution to the Optimal 3D Currents From Remote Scene Sequences project and the Physics Of Coastal Remote Sensing, ARI, at the Naval Research Laboratory, sponsored by the Office of Naval Research.

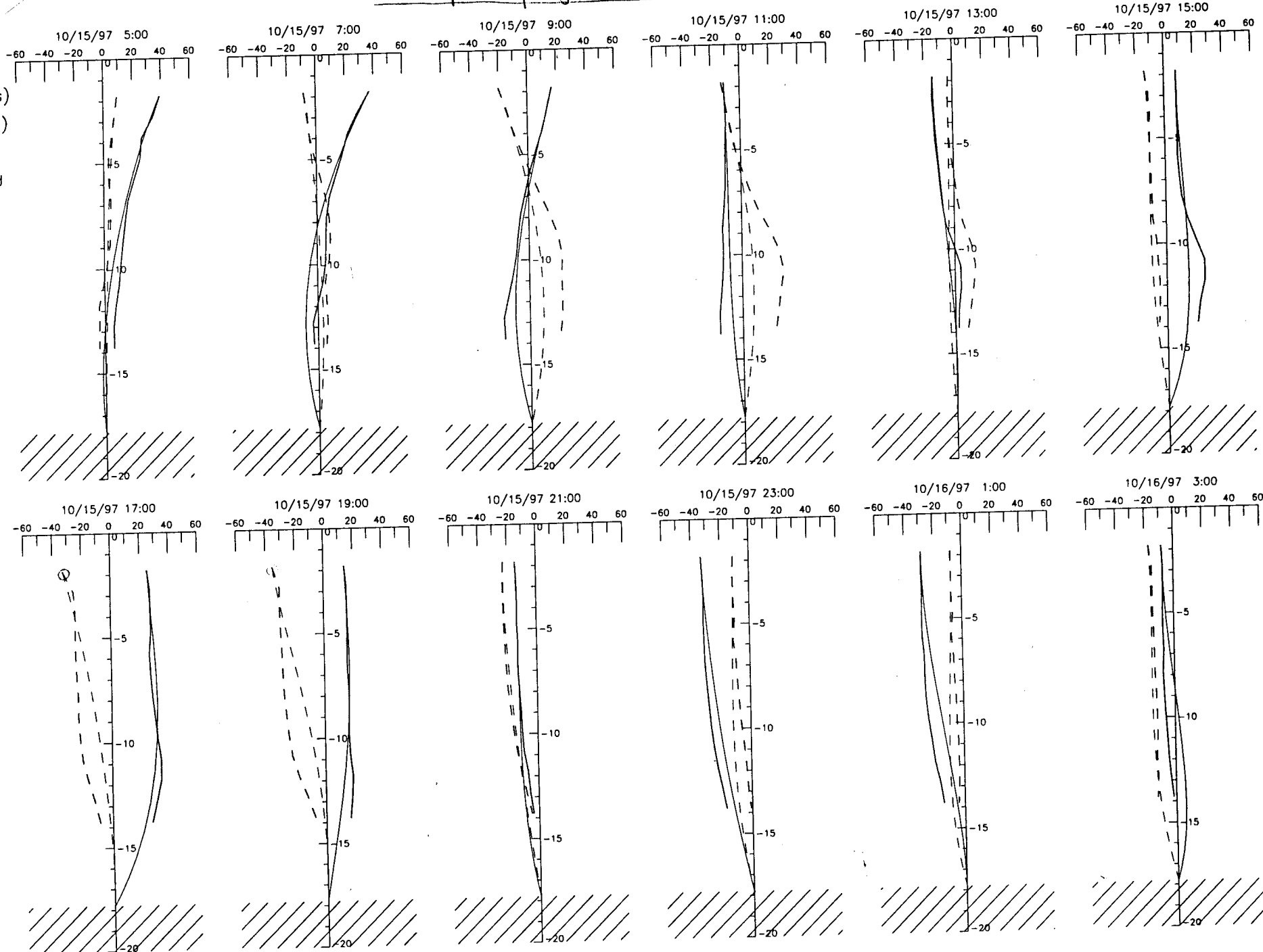
References

- Canuto, C., M. Y. Hussaini, A. Quarteroni, and T. A. Zang, *Spectral Methods in Fluid Dynamics*, Springer-Verlag, New York, 1988.
- Chapman, R. D., L. K. Shay, H. C. Graber, J. B. Edson, A. Karachintsev, C. L. Trump, and D. B. Ross, On the accuracy of HF radar surface current measurements: Intercomparisons with ship-based sensors, *J. Geophys. Res.*, **102**, 18,737–18,748, 1997.
- Davies, A. M., Application of a Galerkin-eigenfunction method to computing currents in homogeneous and stratified seas, in *Numerical Method for Fluid Dynamics*, edited by K. W. Morton and M. J. Bains, pp. 287–301, Academic, San Diego, Calif., 1982.
- Davies, A. M., and G. K. Furnes, Observed and computed M_2 tidal currents in the North Sea, *J. Phys. Oceanogr.*, **10**, 237–257, 1980.
- Davies, A. M., and J. Xing, An intercomparison and validation of a range of turbulence closure schemes used in three dimensional tidal models, in *Quantitative Skill Assessment for Coastal Ocean Models*, *Coastal Estuarine Stud.*, vol. 47, edited by D. R. Lynch and A. M. Davies, pp. 71–95, AGU, Washington, D. C., 1995.
- Fernandez, D. M., J. F. Vesecky, and C. C. Teague, Measurements of upper ocean surface current shear with high-frequency radar, *J. Geophys. Res.*, **101**, 28,615–28,625, 1996.
- Jansen, R. W., C. Y. Shen, S. R. Chubb, A. L. Cooper, and T. E. Evans, Subsurface, surface, and radar modeling of a Gulf Stream current convergence, *J. Geophys. Res.*, **103**, 18,723–18,743, 1998.
- Marmorino, G. O., C. Y. Shen, N. Allan, F. Askari, D. B. Trizna, C. L. Trump, and L. K. Shay, An occluded coastal-oceanic front, *J. Geophys. Res.*, **103**, 21,587–21,600, 1998.
- Mellor, G. L., and T. Yamada, Development of a turbulence closure model for geophysical fluid problems, *Rev. Geophys.*, **20**, 851–875, 1982.
- Mied, R. P., C. Y. Shen, T. E. Evans, and G. J. Lindemann, Frontogenesis with ageostrophic vertical shears and horizontal density gradients: Gulf Stream meanders onto the continental shelf, *J. Geophys. Res.*, **101**, 18,079–18,104, 1996.
- Miller, J. L., M. A. Goodberlet, and J. B. Zaitzeff, Airborne salinity mapper makes debut in coastal zone, *Eos Trans. AGU*, **79**, 173–177, 1998.
- Paduan, J. D., and L. K. Rosenfeld, Remotely sensed surface currents in Monterey Bay from shore based HF radar (CODAR), *J. Geophys. Res.*, **101**, 20,669–20,686, 1996.
- Prandle, D., A new view on near shore dynamics based on observations from H.F. radar, *Prog. Oceanogr.*, **27**, 403–438, 1991.
- Shay, L. K., H. C. Graber, D. B. Ross, and R. D. Chapman, Mesoscale ocean surface current structure detected by HF radar, *J. Atmos. Oceanic Technol.*, **12**, 881–900, 1995.
- Shen, C. Y., Inferring subsurface current structure in a coastal ocean from remote sensing data, in *Proceedings of the Conference on Rapid Environmental Assessment*, edited by E. Pouliquen, A. D. Kirwan, and R. T. Pearson, pp. 83–90, North Atlantic Treaty Org. Supreme Allied Command Atlantic NATO SACLANT Undersea Res. Cent., La Spezia, Italy, 1997.
- Shen, C. Y., R. A. Fusina, and L. K. Shay, An assessment of local coastal dynamics observed with high-frequency radar, *J. Geophys. Res.*, **105**, 6517–6530, 2000.
- T. E. Evans and C. Y. Shen, Code 7250, Remote Sensing Division, Naval Research Laboratory, Washington, DC 20375. (shen@ccf.nrl.navy.mil)

(Received February 10, 2000; revised December 15, 2000; accepted January 12, 2001.)

sample projection results

U (cm/s)
V (cm/s)
True
projected



ADCP4 based at 1.8m (3pt cd; nl = 0.0; $\nu_e = 0.0025$)

(Filter: 6h low-pass: 5min data)